Research Article

Experimental Investigation on Flame Chemiluminescence and Flow Characteristics of a Reverse-Flow Combustor

Ge Hu,[1] **Jianzhong Li** ⓘ**,**[1] **Wu Jin,**[1] **Jingzhou Zhang,**[1] **and Li Yuan**[2]

[1]*Key Laboratory of Aero-Engine Thermal Environment and Structure, Ministry of Industry and Information Technology, Nanjing University of Aeronautics and Astronautics, 29 Yudao St., Nanjing 210016, China*
[2]*School of National Defense Engineering, Army Engineering University of PLA, 88 Biaoying Rd., Nanjing, 210007 Jiangsu, China*

Correspondence should be addressed to Jianzhong Li; ljzh0629@nuaa.edu.cn

The reverse-flow combustor is extensively applied in small engines due to its compact structure. The cold-state flow characteristics, the ignition process, and flame chemiluminescence characteristics of the reserve-flow combustor were investigated experimentally. Using the particle imaging velocimeter, the cold-state time-averaged flow fields at three different total pressure loss coefficients (ζ_B) are examined. The ignition processes of the combustor, as well as flame characteristics during stable combustion at different equivalent ratios (φ), are analyzed based on flame chemiluminescence imaging when ζ_B is 3%. As ζ_B increases from 1% to 5%, the flow field of the combustor remains almost unchanged while the flow velocity increases. For $\zeta_B = 3\%$, the ignition time T drops from 26 ms to 16 ms with an increase of φ. In addition, the ignition performance is enhanced. Proportions of the T2 phase (quasi-stable phase) are 73%, 68%, and 66%, respectively, suggesting that the quasi-stable phase is the key to successful ignition. As φ increases, the flame becomes thinner and shorter. Furthermore, standard deviations of continuous image areas of CH$*$ and OH$*$ drop from 0.0143 and 0.0132 to 0.0115 and 0.0109, respectively, which indicates the enhancement of combustion stability. According to the brightness distributions of CH$*$ and OH$*$ along the axial direction of the combustor at different equivalent ratios, the production of OH$*$ is significantly affected by the temperature. It can be adopted as an important sign of heat release during combustion.

1. Introduction

The combustor of an aero-engine enhances the airflow temperature with the combustion; it should have characteristics such as reliable ignition, stable combustion, and favorable outlet temperature [1]. The flow field of the combustor directly affects the fuel atomization and mixing between fuel and the airflow, which in turn determines ignition and combustion performance. So, it has been the focus of research.

A spray device composed of a matching fuel nozzle and a multi-stage swirl device, usually called a swirl cup, is widely used in aero-engines. A lot of research has been done on the single-head swirl cup model. Mongia et al. [2] studied the influence of pressure and temperature on the time-averaged flow field, as well as the influence of the size of the swirl cup and the structure of the venturi on the flow

field on the CFM-56 aero-engine. Li et al. [3, 4] carried out numerical simulation of the influence of inlet and outlet boundary conditions on the flow characteristics of a three annular cyclone (TARS) and carried out a study on the flow characteristics of the central recirculation zone and the shear layer between the inner and outer flows. Vashahi et al. [5] used the PIV technique to study multi-swirl flow in a rectangular model, comparing the distribution of axial and radial velocities to determine the confinement effects of a rectangular combustion chamber. Most of these studies are limited to straight-flow combustor. However, the airflow in the upper circuit and airflow in the flame tube of the reverse-flow combustor flow in opposite directions. These features make the combustion chamber structure more compact and the length of the engine shortened. It is mainly used in turboshaft engines. The difference in the structure of the reverse-flow
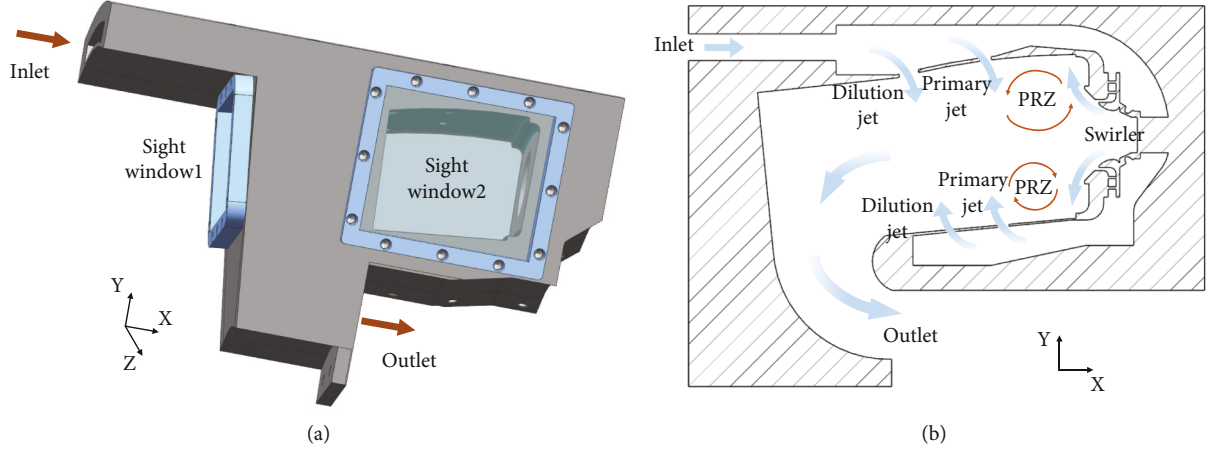
Figure 1: Schematic diagram of the reverse-flow combustor.

combustor and the straight-flow combustor will inevitably lead to differences in the characteristics of flow field and combustion.

Some studies have been carried out on the reverse-flow combustor, such as Reddy et al. experimentally investigated cold-state flow characteristics in the reverse-flow combustor with the pitot tube probe. Moreover, the authors compared the experimental data with numerical calculation results. It was concluded that an increase in the Reynolds number at the inlet can lead to an increase in axial velocity and divergence of radial velocity in the combustor [6–8]. Bharani et al. employed a direction-sensitive pressure probe and standard hot-wire probe to measure the flow field in the reverse-flow combustor. In addition, the authors clarified the flow characteristics of the inlet airflow with different swirling intensities in the outer circular channel of the reserve-flow combustor. Lastly, they investigated the effects on jets from different jet holes [9, 10]. Currently, on account of compact structures, researchers mainly adopt probes and numerical simulations to examine the flow field characteristics and combustion performance in the reverse-flow combustor. However, the mainstream 3D strong rotational flow field test method employs particle imaging velocimeter (PIV) to examine the flow field structure. This method can measure 2D planar flow field based on true condition in the combustor, thereby obtaining the entire flow field structure in the combustor [11–14]. Accordingly, numerical simulation results can be validated by the experimental data. This study reasonably arranged visual optical windows in the reserve-flow combustor model that can satisfy optical path requirements of some measurement instruments such as PIV. The flow field of the reverse-flow combustor is investigated with PIV. For the ignition performance of the combustion chamber, a reasonable flow field is the prerequisite for successful ignition. Favorable ignition performance is also an important index for measuring combustor performance. Lefebvre et al. conducted a significant number of investigations on the ignition performance of a combustor [15–17]. Based on the model of the premixed combustion chamber, the authors investigated both ignition and flame propagation mechanisms and extracted the characteristics

Table 1: Geometrical parameters of the jet holes ("Δ" refers to a round hole, "Λ" refers to semicircle hole).

		Primary holes	Dilution holes
Arrangement	Top	$\Delta-\Delta-\Delta$	$\Lambda-\Delta-\Lambda$
	Bottom	$\Lambda-\Delta-\Lambda$	$\Delta-\Delta$
Axial distance (mm)	Top	34	22.5
	Bottom	65	49

at different development phases of ignition [18]. Philip et al. validated the test results via large-eddy simulation (LES) calculation and further analyzed different ignition stages in detail [19]. Prieur et al. focused on the effects of equivalent ratio and flow velocity on the ignition time. The authors found that fuel distribution plays an important role in both the propagation and stabilization of flames [20]. Chemiluminescence combustion refers to the luminescence at a particular wavelength when free radicals excited in combustion chemical reaction transit from high- to low-energy levels; It is easy to use under severe environments without high-power laser and complex light paths [21, 22]. In hydrocarbon fuel, leading chemiluminescence behaviors are obtained by CH * and OH * at 430 nm and 307 nm, respectively. The main reaction mechanisms are described as follows:

$$C_2H + O \leftrightarrow CH * + CO, \tag{1}$$

$$CH + O_2 \leftrightarrow OH * + CO. \tag{2}$$

CH * and OH * show different characteristics in the chemical reaction. These elements are extensively applied when determining chemical zones, identification of heat release, and evaluation of combustion equivalent ratio [23–25]. Higgins et al. investigated the relations of chemiluminescence of OH * with pressure and equivalent ratio, which expanded the application range of chemiluminescence [26]. Hardalupas et al. measured chemiluminescence imaging and examined the characteristics of premixed flames of natural gas at different equivalent ratios. The
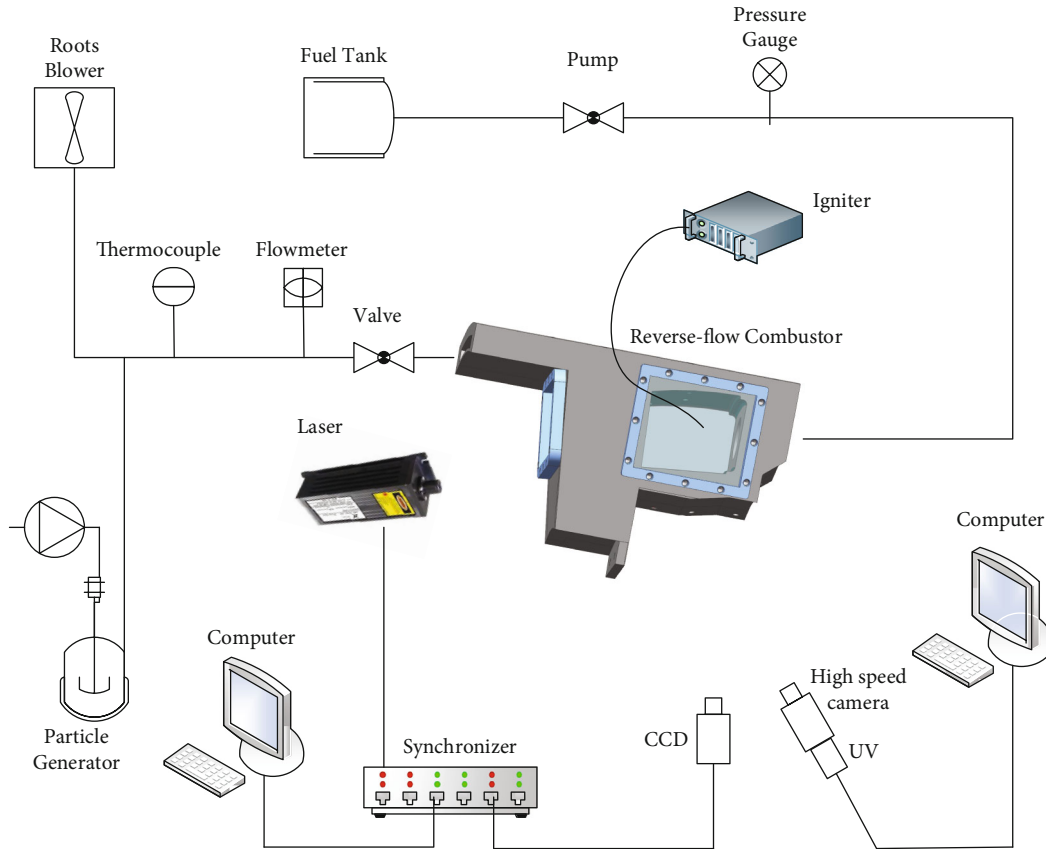
FIGURE 2: Schematic of the experiment system.

TABLE 2: Parameters of the experiment.

T_3/K	P_{t3}/Pa	(ζ_b)	φ
300	101325	1%/3%/5%	0.6/0.66/0.72

authors concluded that $OH*$ and $CH*$ are important markers of heat release rate [27]. Garcia et al. indicated application prospects of $OH*/CH*$ chemiluminescence when evaluating the distribution of the equivalent ratio of the combustor [28]. Orain et al. focused on the effects of equivalent ratios and different fuel compositions on the heat release rate. Moreover, the authors measured $OH*$, $CH*$, and $C2*$ via chemiluminescence imaging [29]. According to their results, different fuel compositions differ in the optimal marker of heat release rate.

The previous studies exhibit important guidance for exploring flow, ignition, and combustion characteristics. In this study, based on the reserve-flow combustor model, the inner flow field structure was measured with PIV, and the ignition process, as well as flame characteristics, was examined using flame chemiluminescence imaging. The present study can deepen the understanding of flow, ignition, and combustion process in a reverse-flow combustor.

2. Combustor Model and Experiment System

2.1. Reverse-Flow Combustor Model. The fan-shaped reserve-flow combustor is shown in Figure 1(a). Figure 1(b) shows a typical flow structure diagram of reverse-flow combustor. More details of the model combustion chamber can be found in [30], but the axial position and layout of the upper and lower jet holes are different from the structure used in [30]. Table 1 shows the parameters of jet holes.

2.2. Experiment Parameters. The experiment system is shown in Figure 2; it mainly consists of the reverse-flow combustor, the air supply system, the fuel system, and the measurement system. Further, the measurement system includes PIV measurement system and spontaneous radiation measurement system. Sampling rakes were arranged to measure inlet total pressure (P_{t3}) and outlet total pressure (P_{t4}) with a maximum error of 0.2%, and inlet total temperature (T_3) with a maximum error of 0.4%. The inlet mass flow rate (W_{air}) was measured by the LUGB/E vortex shedding flowmeter with a maximum error of 1%. The fuel pump was used to support the liquid fuel *of RP-3 kerosene.* The fuel mass flow rate (W_{fuel}) is measured through the pressure drop of the atomizer. The relationship between the flow rate and the pressure drop is fitted as:

$$W_{fuel} = 0.45\Delta P_{fuel}^{0.497}. \tag{3}$$

The ignition electronic nozzle was arranged on the side-wall of the single-head combustor, which was 2 mm away from the sidewall. The PIV system was made up of a Bobcat B2041 digital camera. An Nd:YAG double-pulse laser with a
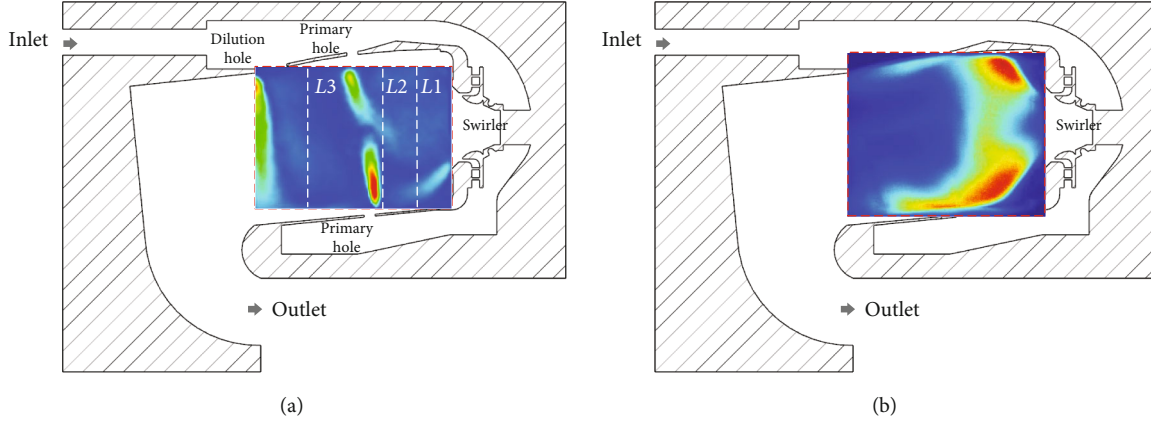
(a)

(b)

FIGURE 3: Measurement area of P0 section: (a) cold-state flow field experiment and (b) combustion experiment.

TABLE 3: Relevant values of uncertainties in experiments.

Parameter	Description	Error (%)
Pressure loss	$\zeta_B = (P_{t3} - P_{t4})/P_{t3}$	≤0.35
φ	$\varphi = W_{\text{fuel}}/(W_{\text{air}}\text{FAR}_{\text{ST}})$	≤0.5

laser wavelength of 532 nm, maximum single-pulse energy of 200 mJ, and a maximum operating frequency of 15 Hz was used. A MicroPulse 725 synchronous controller was used to control the camera, the laser, and the image capturing board [31]. The essence of PIV measurement is to characterize the flow structure by acquiring the flow characteristics of the tracer particles. Stokes number (Stk) is introduced as the criterion for selecting tracer particles [32]. Stk is the ratio of particle relaxation time to fluid characteristic time, which represents the ratio of particle inertia and diffusion. The calculation formula is:

$$\text{Stk} = \frac{\tau_f}{\tau_p}, \tag{4}$$

where τ_p is the reaction time of the tracer particles, and τ_f is the characteristic time of the flow. When Stk < 1, the diffusion of particles is more dominant than the inertial force, and the PIV test results are more credible. So, the tracer particles were introduced at a position 1 m upstream of the intake section, and MgO particles with a particle size of 5 μm were selected as tracer particles in this study to ensure Stk < 1.

The total pressure loss directly affects the performance of the engine. The total pressure loss coefficient (ζ_b) is one of the important parameters to characterize the state of the combustor. It can be calculated by:

$$\zeta_B = \frac{(P_{t3} - P_{t4})}{P_{t3}}. \tag{5}$$

The parameters of the experiment are shown in Table 2.

Due to the fact that the laser plane and the CCD camera viewing plane are perpendicular to each other in the PIV experiment, the actual measurement area of flow field at the center section P0 of the combustor is shown in Figure 3(a). Here, $L1$, $L2$, and $L3$ denote the position lines at different axial distances from the outlet of the swirler ($L1 = 10$ mm, $L2 = 20$ mm, and $L3 = 40$ mm). The origin of the coordinate system is located at the lower left corner of the measurement area, and the positive direction of X axis is the same as the direction of the inlet velocity of the combustor, and opposite to the direction of the main flow inside the reverse-flow combustor.

The spontaneous radiation system adopts the combination of Phantom V2012 high-speed camera and Invisible version UVi image intensifier, equipped with Nikon 50 mm fixed focus lens, to capture high frame rate images of ignition process and CH ∗ and OH ∗ image during stable combustion process. The CH ∗ filter with a wavelength of 430 nm and a bandwidth of 5 nm as well as an OH ∗ filter with a wavelength of 307 nm and a bandwidth of 5 nm was arranged in front of the camera. Since CH ∗ and OH ∗ are imaged via the filters at particular wavelengths with fairly low light transmittance outside the bandwidth range, the effects of some particles, such as soot, on the measurement of CH ∗ and OH ∗ can be neglected. In view of the structure of the combustor model and the framing characteristics of the camera, the actual measurement area of the flame at the central section P0 is shown in Figure 3(b). The sampling frequency was set to 2 000 Hz. 8-bit grayscale images were obtained. The pixels were calibrated before image acquisition. Finally, images with a resolution of 630 ∗ 550 were obtained [33].

2.3. Experimental Error Analysis. Errors generated in the test process can be calculated according to the following formula [34, 35]:

$$\Delta R = \left[\left(\frac{\partial R}{\partial x_1}\Delta x_1\right)^2 + \left(\frac{\partial R}{\partial x_2}\Delta x_2\right)^2 + \cdots + \left(\frac{\partial R}{\partial x_n}\Delta x_n\right)^2 \right]^{1/2}, \tag{6}$$

where ΔR is the uncertainty of the derived physical quantity;

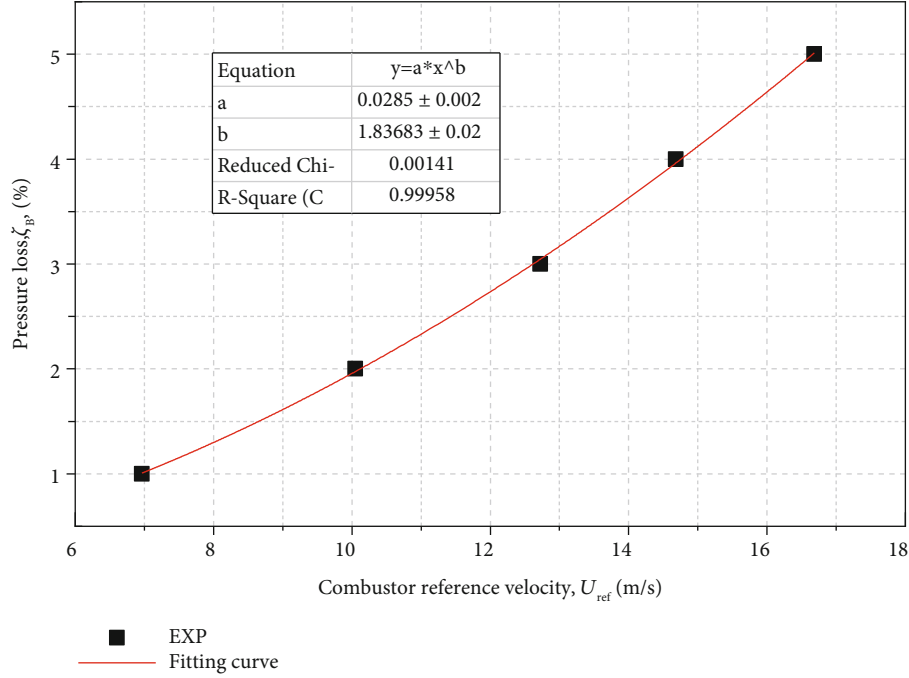| Equation	y=a*x^b
a	0.0285 ± 0.002
b	1.83683 ± 0.02
Reduced Chi-	0.00141
R-Square (C	0.99958

- ■ EXP
- —— Fitting curve

FIGURE 4: Effect of combustor reference velocity on total pressure loss.

$(\partial R / \partial x_n) \Delta x_n$ is the uncertainty corresponding to each measurement parameter.

Taking the uncertainty of the equivalence ratio (φ) as an example, the calculation formula of φ is:

$$\varphi = \frac{W_{fuel}}{(W_{air} FAR_{ST})}. \tag{7}$$

Here, FAR_{ST} is the stoichiometric ratio of RP-3 kerosene. $FAR_{ST} = 0.067$. According to formula (6) and (7), the uncertainty of φ is calculated as:

$$\Delta R_\Phi = \sqrt{\Delta R_{fuel}{}^2 + \Delta R_{air}{}^2}, \tag{8}$$

where ΔR_{air} and ΔR_{fuel} are the uncertainties of W_{air} and W_{fuel}, respectively.

Table 3 shows the relevant values of uncertainties in experiments.

3. Results and Discussions

3.1. The Flow Field. The experiment was conducted at inlet static pressure 101 kPa and the temperature 300 K. The results and a fitting curve are shown in Figure 4. The pressure loss increases with the reference velocity (U_{ref}) increasing. The largest pressure loss under experiment operations which is fixed at the maximum combustor inlet velocity (16.7 m/s) is 5%. The fitting curve is defined as:

$$\zeta_B = 0.029 U_{ref}^{1.84}, \tag{9}$$

where the R-Square is 0.999, which means the fitting curve is

in accord with the experiment results ideally. So the higher the reference velocity is, the more drastic the total pressure loss changes.

The cold-state time-averaged flow fields at section P0 of the reverse-flow combustor with different ζ_B values were measured by PIV. Figure 5 shows the cold-state time-averaged flow fields at section P0 when $\zeta_{B1} = 1\%$, $\zeta_{B2} = 3\%$, and $\zeta_{B3} = 5\%$. The flow fields at section P0 under different ζ_B values show similar structures with almost identical vortex positions, jet penetration depths, and flow lines. The vortex center positions of the vortex in the primary recirculation zone (primary vortex) and the vortex formed after the collision of the primary hole jets (secondary vortex) are recorded as R and S, respectively. The positions of R and S under different ζ_B values are shown in Table 4. It means ζ_B has little effect on the flow field structure.

Figure 6 displays the distribution of u and v at different axial distances ($L = 10$, 20, and 40 mm). The values of u and v can be normalized by u_{max}; u_{max} is the U_{ref} when ζ_B is 5%. The effect of ζ_B imposes consistent effects on flow structure at any axial positions, suggesting the irrelevance of the flow field structure to the inlet condition of the combustor. However, the ζ_B value at the inlet can lead to an increase in the flow velocity. At $L1 = 10$ mm, radial height in the central recirculation zone at the axial distance can be reflected by the axial velocity component u at $y \approx 6$-20 mm. Moreover, when $y < 20$ mm, both velocity components u and v show low-velocity and high-velocity flow alternation along the radial direction. This can increase both u and v gradients and strengthen the flow mixing action. When $y > 20$ mm, u and v change gently along the radial direction. At $L2 = 20$ mm, the radial height of the central recirculation zone increases, and it is accompanied by a large-gradient flow of
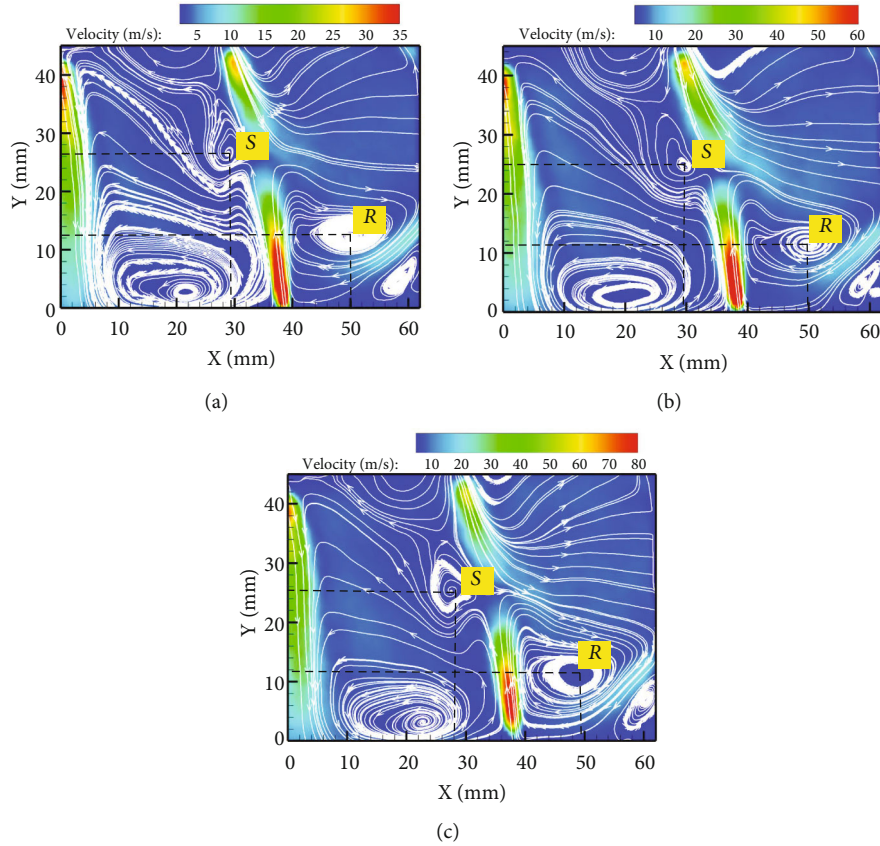
(a)

(b)

(c)

FIGURE 5: Cold-state time-averaged flow fields at section P0 under different conditions: (a) ζ_B =1%, (b) ζ_B =3%, and (c) ζ_B =5%.

TABLE 4: The vortex center location of the primary vortex and secondary vortex.

ζ_B/location	Primary vortex (R)		Secondary vortex (S)	
	X (mm)	Y (mm)	X (mm)	Y (mm)
1%	50	12	29	26
3%	50	11.5	29	25
5%	49.5	12	28	26

u and v. When y >15 mm, the gradient of v further increases. However, basic flow characteristics remain almost unchanged. At $L3 = 40$ mm and $y \approx 4$-36 mm, i.e., the primary zone of the combustor, flow moves smoothly to the combustor downstream, while the flow velocity near both upper and lower wall sizes varies significantly. This is mainly because a large adverse pressure gradient exists near the downstream wall of upper and lower primary holes, thereby producing local vortexes.

3.2. Ignition. It can be found that ζ_B has a slight effect on the flow field of the reverse-flow combustor through the research in the previous section. The spontaneous radiation experiments were conducted at ζ_B =3%.

The ignition process of the combustor was recorded. The equivalence ratio of the combustor was adjusted by adjusting the valves in the fuel supply pipeline to supply fuel with different mass flow rates. In order to highlight the details of the

image and improve the anti-interference capability of the image, the grayscale images of flame obtained by the high-speed camera were converted into pseudo-color images through Matlab software. The typical flame development diagrams during the ignition process of the reverse-flow combustor are shown in Figure 7.

It can be assumed that the flame's illumination intensity during the ignition process can reflect the instantaneous heat release rate of the combustion. Furthermore, by taking integral of the illumination intensities of various pixels in the gray-level images during the ignition process, variation of the illumination intensity per unit pixel with time can be obtained, as shown in Figure 8.

The ignition process of the reverse-flow combustor can be divided into three phases [36]. In the first turbulent dissipation phase, the high-energy spark plug discharges, evaporating and igniting the mixed gas. Flame intensity drops gradually to form the initial flame nucleus. At the same time, the followability of small-sized droplet particles is better, and better mixing is formed in PRZ, so the initial flame nucleus near the PRZ. Next, the second phase is the quasi-stable phase. A low-velocity recirculation zone is conducive for the formation and stabilization of the initial flame. At this phase, fresh mixed air entertained by the recirculating vortex absorbs energy. Simultaneously, the initial flame nucleus gradually develops along with the recirculating vortex, thereby leading to steady heat release. During the entire process, heat release is first slightly lower than heat loss. Then,
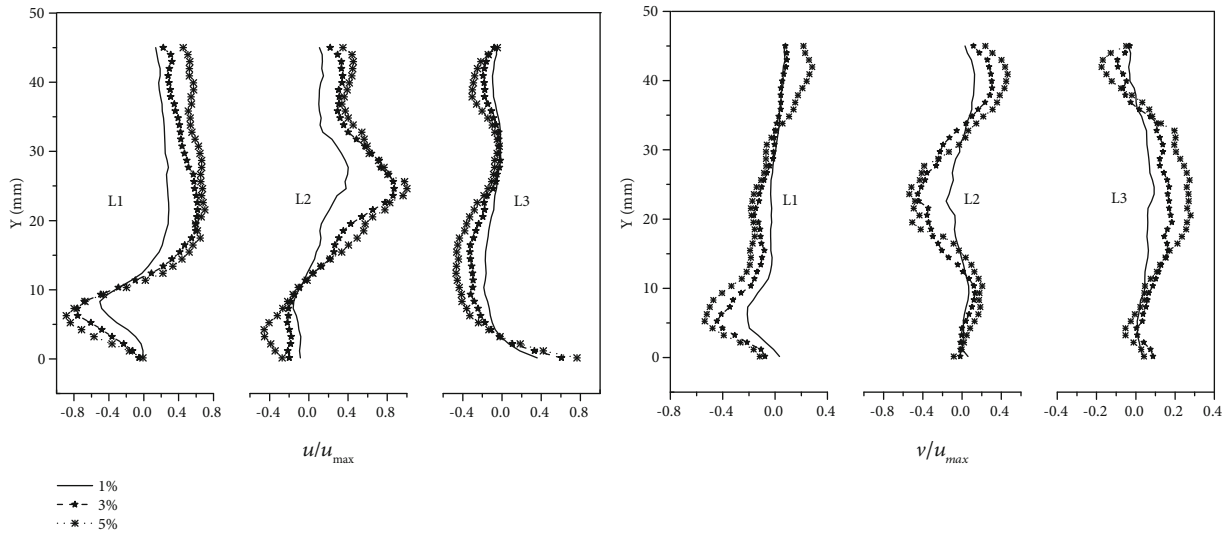
FIGURE 6: Distribution patterns of u and v at different axial positions.
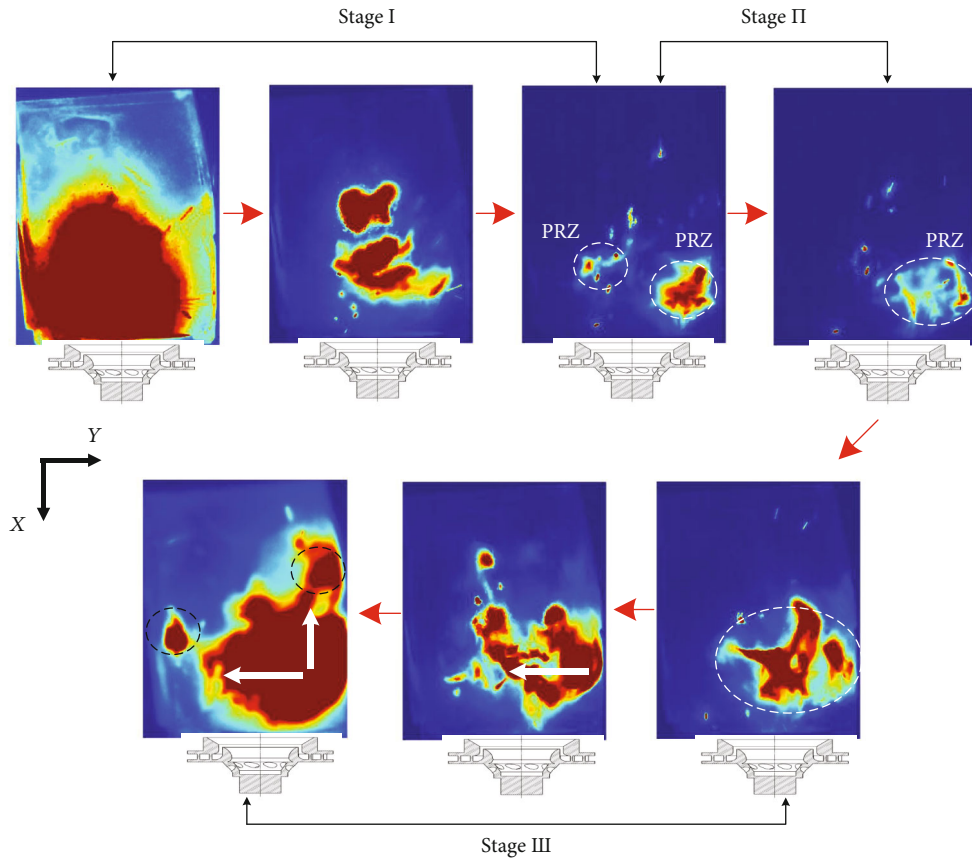

FIGURE 7: Ignition process of the combustor (by rotating the flame image clockwise by 90°).

with the development of the initial fire nucleus, heat release slightly exceeds the heat loss, thereby resulting in gradual energy accumulation. Finally, flame develops to stable combustion state, and the combustor ignites successfully at the third combustion-enhanced phase. The flame expansion first occurs in PRZ. The chemical reaction is enhanced with the continuous flame expansion, and the temperature of the unburned air-fuel mixture near flame and the fuel evaporation rate are greatly increased. At the same time, the rapid increase of unburned air-fuel mixture temperature and fuel evaporation rate will further promote the enhancement of chemical reaction. Flame expands rapidly under the action of this pair of positive feedbacks, and the flame develops from the upper PRZ to the lower PRZ. Finally, the
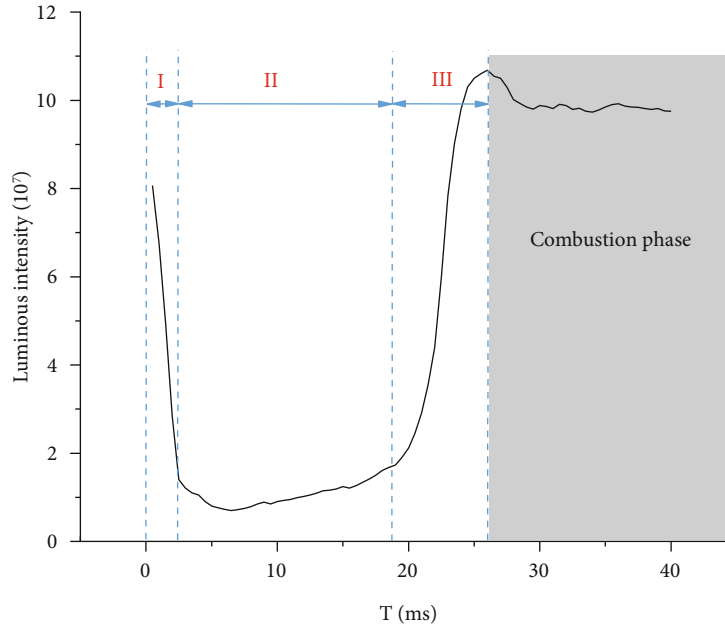
Figure 8: Variation of the integral f illumination intensity with time.

Table 5: Ignition times under different operating conditions.

φ	T_1 (ms)	T_2 (ms)	T_3 (ms)	T (ms)
0.6	2	19	5	26
0.66	2	13	4	19
0.72	2	10.5	3.5	16

combustor is successfully ignited. The combustion chemical reaction continues to be transmitted downstream and ignites the entire combustion chamber rapidly to achieve stable combustion with the action of turbulent dissipation; the flame intensity increases to a peak value and tends to be stable. The total ignition T can be calculated as $T = T1 + T2 + T3$, where $T1$, $T2$, and $T3$ denote the durations of three phases.

Table 5 lists the distributions of $T1$, $T2$, and $T3$ during the ignition process at different equivalent ratios when ζ_B =3%. The combustor can be successfully ignited at three different equivalent ratios. Moreover, the total ignition delay time T decreases with the enhancement of equivalent ratio, accompanied by the enhancement of ignition performance. To be specific, $T1$ remains almost unchanged since the first phase is mainly affected by the energy of the high-energy igniter itself. As the equivalent ratio increases, $T2$ drops by 31.6% and 44.7%, while $T3$ is reduced by 20% and 30%. The second and third phases are closely correlated with fuel/gas spatial distribution. Accordingly, the increasing equivalent ratio increases the fuel mist concentration in the combustor, which can significantly change the ignition times in the latter two phases. Under three operating conditions, the second phase occupies a dominant role in the entire ignition process. Proportions of $T1$ in three phases are 73%, 68%, and 66%, while the duration of the quasi-stable phase decreases slightly with an increase in the equivalent ratio.

Therefore, the second phase imposes a significant effect on successful combustor ignition. By combining the cool-state time-averaged flow field in Figure 4, the flame mainly stays in the central recirculation zone. Furthermore, flow velocity in the recirculation zone is low, and fresh air can be constantly supplemented, thereby leading to constant energy accumulation. As energy is accumulated to a certain degree, combustion can be gradually enhanced. Afterward, flame develops steadily in the central recirculation zone, becomes more intensive, and moves downstream towards the combustor. Finally, the combustor can be successfully ignited. Therefore, flow structure significantly affects the ignition performance of the combustor. It can be concluded that favorable flow structure design is of great significance.

3.3. Chemiluminescence. CH ∗ is tightly related to the combustion reaction and OH ∗ can be used to obtain heat release characteristics. Distributions of intermediate products CH ∗ and OH ∗ during stable combustion in the combustor at different equivalent ratios were measured via spontaneous radiation imaging. After cropping, filtering, and normalization on the original flame images via spontaneous radiation imaging, the continuous image series taken under each operating condition were averaged because of strong turbulent flame pulses. The averaged image represents a stable combustion image under the corresponding operating conditions. Finally, the image boundary was extracted by taking pseudo-color processing and OSTU algorithm [31], as shown in Figure 9.

During the combustion of hydrocarbon fuel, a tight correlation between CH ∗ and combustion reaction can be confirmed. Therefore, the distribution of CH ∗ can be used for reflecting the flame structure. Figure 10 shows the distributions of CH ∗ at three different equivalent ratios as well as the comparison of boundary contours. It can be observed
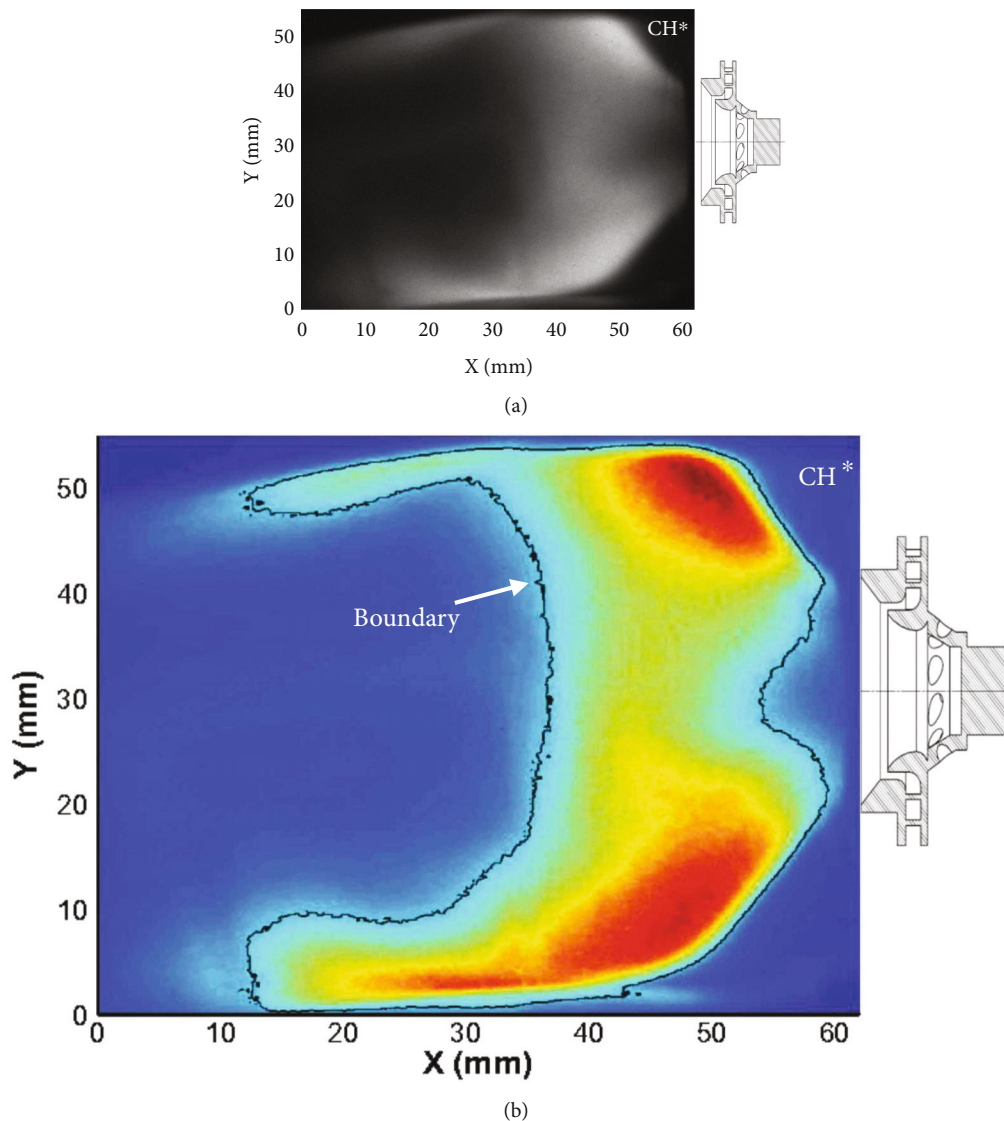
(a)

(b)

FIGURE 9: Image processing method: (a) original image and (b) post-processing image.

that flames at different equivalent ratios show almost unchanged contour features. Based on the contour, the flame image can be divided into the flame development zone (Zone 1), complete combustion zone (Zone 2), and combustion wake zone (Zone 3). In Zone 1, the flame front develops downstream towards the combustor in a V-shaped pattern with an expansion angle of approximately 80°. The flame can be radially extended to the height of the flame tube, exhibiting typical non-premixed diffusion combustion characteristics. This suggests that the change of equivalent ratio imposes a minor effect on the flame's initial expansion angle. The expansion angle mainly depends on the spray cone angle of the centrifugal nozzle. In Zone 2, the flame undergoes complete combustion and spreads to the entire flame tube. High-brightness zones near the upper and lower wall surface can be observed. However, the upper and lower high-brightness zones show different contour characteristics that correspond to the edges of the upper and the lower recirculation zones in the flow field. This can be attributed

to the asymmetry of the jets from upper and lower primary holes due to the different axial positions of these two primary holes in the reverse-flow combustor. The jets from primary holes truncate the primary flow and interact with the rotational flow, thereby forming asymmetrical upper and lower primary recirculation zones in the head part. The recirculating vortex promotes the mixing between the fuel and the fresh air. On the other hand, due to the low velocity of the recirculating vortex, the retention time of fuel can also be prolonged with violent combustion. Moreover, the flame is truncated due to the truncation of jets from primary holes. Due to upper and lower recirculating vortexes, a small part of fuel and gas still spreads downstream. This reduces the local equivalent ratio and weakens the flame intensity. In the combustion wake region, combustion flames move downstream near the wall surfaces, where flame intensity is significantly weakened. This is because a small portion of unburned fuel moves downstream with the primary flow after the combustion in the primary zone. Furthermore, flow
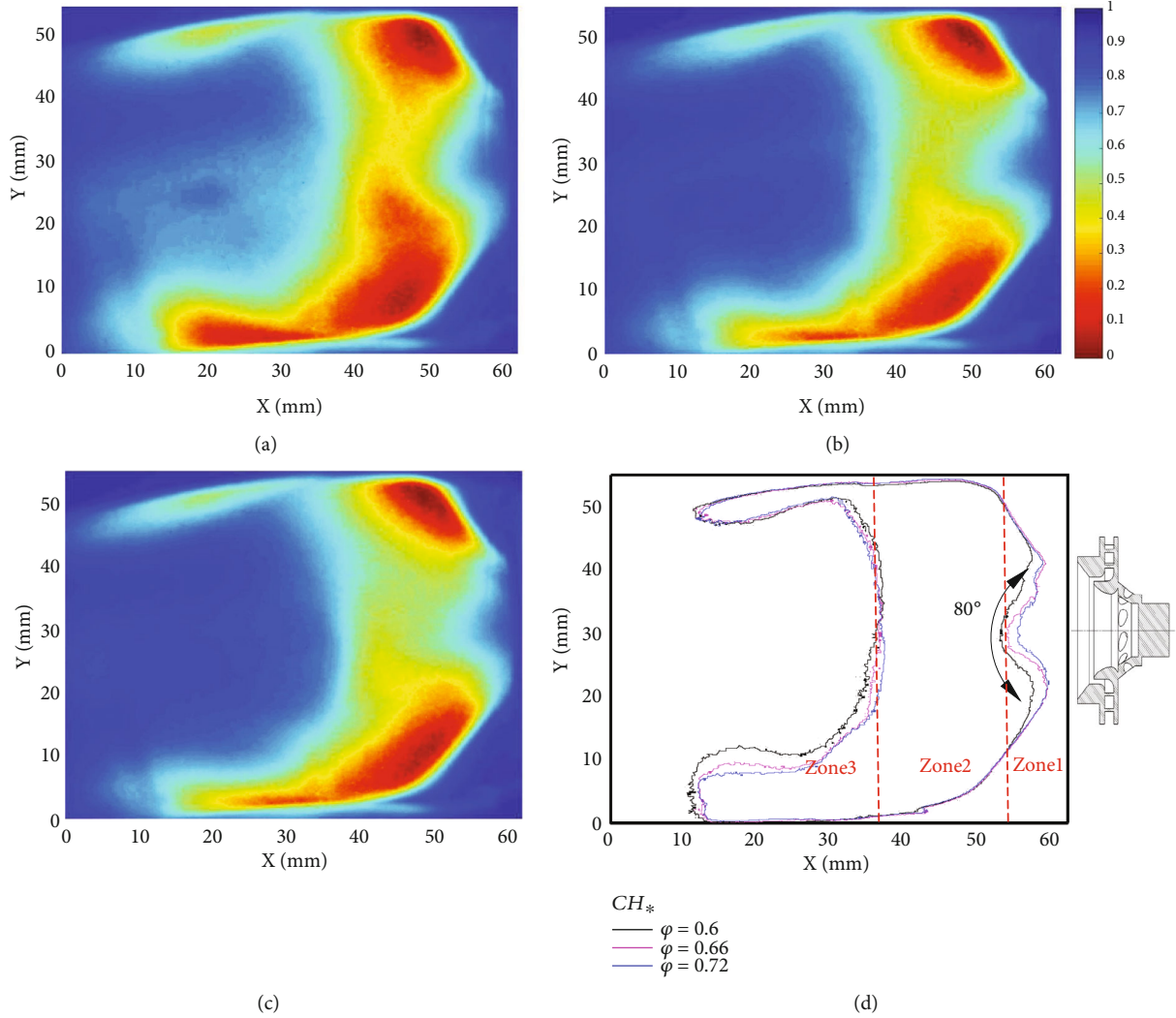
(a)

(b)

(c)

CH_*
—— $\varphi = 0.6$
—— $\varphi = 0.66$
—— $\varphi = 0.72$

(d)

FIGURE 10: Distributions of CH *chemiluminescence image: (a) $\varphi=0.6$, (b) $\varphi=0.66$, (c) $\varphi=0.72$, and (d) boundaries of CH * chemiluminescence image.

pressure around the high-velocity jet column of upper and lower main holes drops, which leads to vortex flowing downstream near the wall of the main hole. This can provide necessary flow conditions for stable combustion, which is consistent with the flow field structure shown in Figure 5. In addition, as the equivalent ratio increases, the fuel distribution concentration increases, the combustion reaction can be accelerated, and the flame front moves forward. Furthermore, the reaction intensity in the combustion wake zone increases and the flame stabilizes. Accordingly, the flame in the Zone 3 becomes thinner and shorter.

Based on the extracted boundary contours of averaged CH * and OH * images, the areas of CH * and OH * at three different equivalent ratios can be calculated and normalized according to the area of the entire image:

$$S = \sqrt{\frac{\left[(x_1 - \bar{x})^2 + (x_2 - \bar{x})^2 + \cdots + (x_n - \bar{x})^2\right]}{n}}. \quad (10)$$

Standard deviation (S) of the areas of two intermediate products in continuous image series at different operating conditions (Figure 11) is calculated as $S = S_0/S_A$. Overall, as φ increases (the combustor is still under lean oil combustion at that moment), the reaction can be accelerated, and fuel undergoes complete combustion. This leads to a decline in flame length and the thinning of the flame surface. Accordingly, the proportion of areas of two combustion intermediate products decreases, i.e., the areas of CH * and OH * gradually drop with an increase in the equivalent ratio. As the equivalent ratio increases, the combustion is enhanced, both reaction and heat release effect become more compact and stable, and the ratios of OH * area to CH * area at three equivalent ratios are increased by 3.67%, 3.02%, and 2.13%, respectively. The standard difference of the intermediate product area proportion in continuous image series, denoted as S, can be used for reflecting the difference between combustion stability and various operating conditions at different equivalent ratios. Since the turbulent combustion in the combustor is a non-steady process, random vortexes are
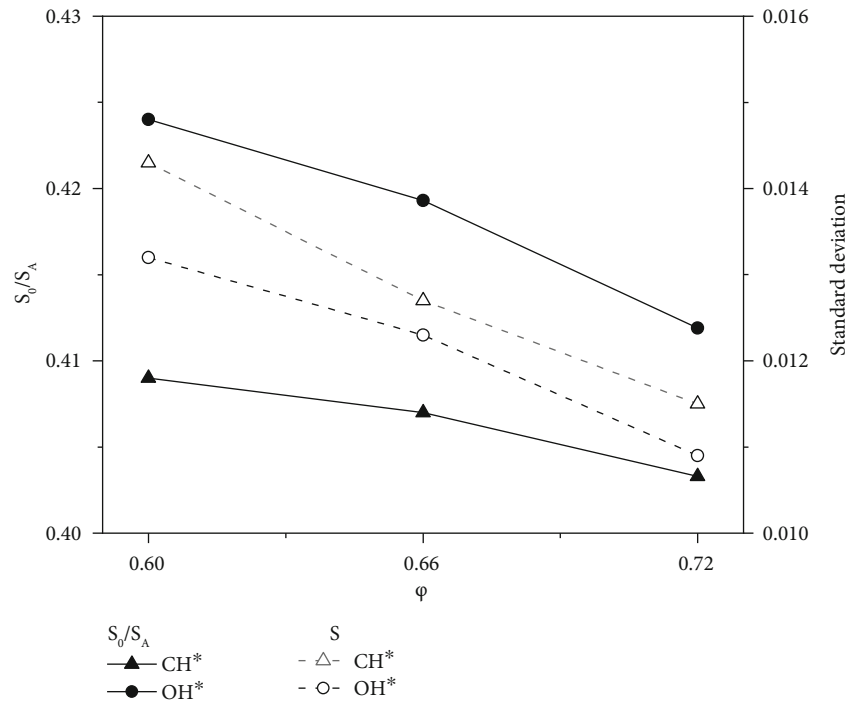
FIGURE 11: Area and standard deviation of the reaction zone and the heat release zone.
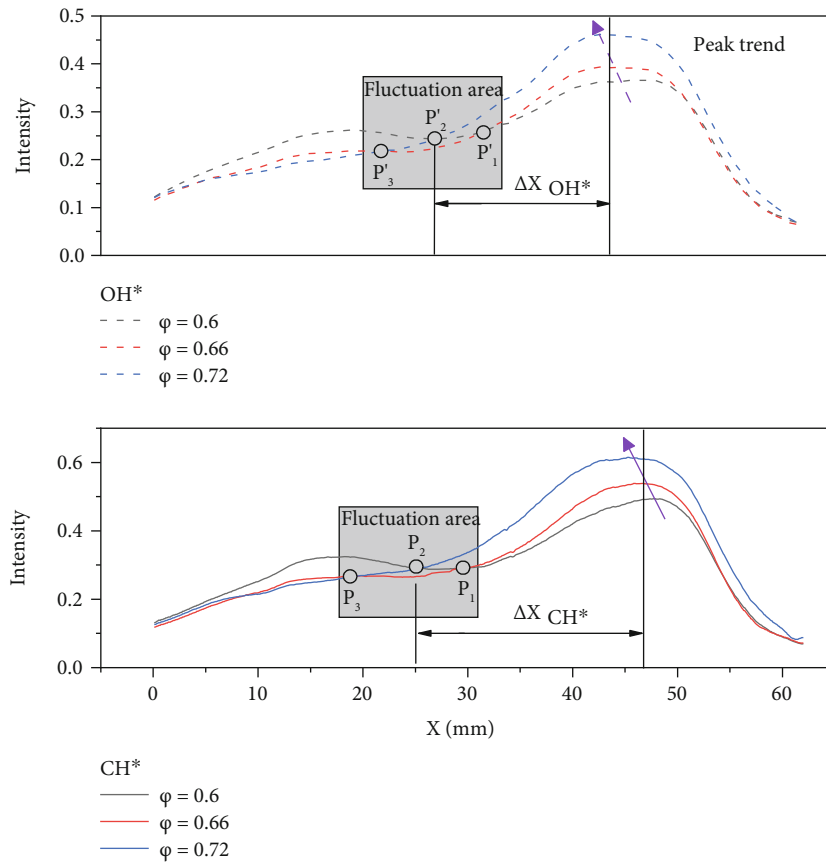

FIGURE 12: Distribution of chemiluminescence intensity along the axial direction.

produced under the interaction between the jest from primary holes and the rotational flows in the head. This can impose disturbance on the combustor flames, thereby affecting both reaction and heat release zones. As the equivalent ratio increases, the standard deviations of continuous image areas of CH ∗ and OH ∗ drop from 0.0143 and 0.0132 to 0.0115 and 0.0109, respectively. This suggests that the combustion stability is enhanced with an increase in the equivalent ratio. Heat release hysteresis is present compared with combustion chemical reaction, and it is subjected to multiple factors including energy, turbulent dissipation, and thermal radiation. Therefore, the standard deviation of the heat release zone is smaller than the one of the reaction zone. Thus, it can be concluded that equivalent ratio change affects the sizes of the combustion reaction zone, heat release zone, and combustion stability under the same airflow conditions.

By applying the normalization process on the brightness of all pixels in time-averaged images at different equivalent ratios, the brightness distributions of CH ∗ and OH ∗ along different axial directions of the combustor at different equivalent ratios are obtained, as shown in Figure 12. Since the combustion in the primary recirculation zone is most intense and it weakens downstream along with the combustion, the mean brightness of CH ∗ and OH ∗ first increases and then drops from the outlet of the swirler to the downstream direction of the combustor. Brightness distributions of CH ∗ and OH ∗ also fluctuate. In the upstream of the fluctuation zone (i.e., the primary combustion flame zone), the mean brightness of CH ∗ and OH ∗ at different axial positions increases with the equivalent ratio. This may be because the increasing equivalent ratio can intensify the chemical reaction, thereby leading to an increase in the spontaneous radiation intensities of CH ∗ and OH ∗. Since the fluorescence signal of the spontaneous radiation of CH ∗ is higher than that of OH ∗ under the same conditions, the intensity of CH ∗ exceeds that of OH ∗ at the same axial position. In addition, two among three curves in the fluctuation zone are intersectant. The intersection points along the flow direction in the combustor are denoted as P1, P2, and P3. By taking Point P2 as the reference point, the distance between the axial position corresponding to the curve peak and the axial distance between the axial position corresponding to the curve peak and P2 is denoted as ΔX. It can be observed that ΔX_{CH*} is larger than ΔX_{OH*}. On the one hand, the position of OH ∗ peak lags behind that of CH ∗ peak. Moreover, as the flame propagation intensity weakens towards the downstream part of the combustor, the corresponding axial position of OH ∗ in the fluctuation zone moves more forward than the position of CH ∗. This suggests that the production of OH ∗ is significantly affected by the temperature. Accordingly, OH ∗ can be adopted as an important sign of combustion heat release.

4. Conclusions

This study experimentally investigated the flow field, ignition, and flame structure characteristics of a reverse-flow combustor. The following conclusions can be drawn:

(1) As total pressure loss coefficient (ζ_B) varies from 1% to 5%, the flow in the combustor is under a self-modeling state. The time-averaged flow field structure remains almost unchanged. However, the flow velocity in the combustor is increased

(2) When ζ_B =3%, the ignition time T decreases from 26 ms to 16 ms as the equivalent ratio increased, suggesting the enhancement of ignition performance. The entire ignition process can be divided into three phases: turbulent dissipation phase, quasi-stable phase, and combustion-enhanced phase. The change of φ mainly affects the times consumed in the quasi-stable phase and the combustion-enhanced phase (T2 and T3), respectively. In particular, the quasi-stable phase is an important factor that determines whether the combustor can be successfully ignited. As φ increases from 0.6 to 0.66 and 0.72, T2 drops by 31.6% and 44.7%, respectively. On the other hand, T3 can be reduced by 20% and 30%, respectively. And it can be founded that flow field of the combustor is tightly correlated with ignition performance and flame propagation behavior

(3) The distribution of CH ∗, with close relation to the combustion reaction, can be used for characterizing the flame front position. An increase in the equivalent ratio can intensify the chemical reaction and enhance combustion stability, resulting in a decrease of CH ∗ and OH ∗ areas. Standard deviations of the continuous image areas of CH ∗ and OH ∗ drop from 0.0143 and 0.0132 to 0.0115 and 0.0109, respectively. For the same equivalent ratio, the axial position of OH ∗ peak point moves backward further than the axial position of the CH ∗ peak point. Moreover, the axial position corresponding to OH ∗ in the fluctuation zone moves more forward than the axial position of CH ∗. This suggests that the distribution of OH ∗ is significantly affected by temperature. As such, it is an important sign of heat release in combustion

Nomenclature

PIV: Particle image velocimetry
φ: Equivalence ratio
W_{fuel}: Fuel mass flow rate
FAR: Fuel-air ratio
P_{t3}-P_{t4}: Inlet/outlet total pressure
ζ_B: Liner pressure loss
PRZ: Primary recirculation zone
RP-3: One kind of liquid kerosene
W_{air}: Air mass flow rate
FAR_{ST}: Stoichiometric ratio
u_{max}: Inlet velocity at ζ_B with 5%.

Data Availability

The data used to support the findings of this study are available from the corresponding author upon request.

Conflicts of Interest

Acknowledgments

References

[1] H. Mongia, "Engineering aspects of complex gas turbine combustion mixers part II: high T3," in *49th AIAA Aerospace Sciences Meeting including the New Horizons Forum and Aerospace Exposition*, Orlando, Florida, January 2011.

[2] H. Mongia, M. Al-Roub, A. Danis et al., *Swirl Cup Modeling Part 1*, 2001.

[3] G. Li, S. Angier, O. Lambolez, E. Gutmark, and B. Drouin, "Experimental study of velocity flow field for a multiple swirl spray combustor," in *40th AIAA Aerospace Sciences Meeting & Exhibit*, Reno, NV, 2002.

[4] G. Li and E. J. Gutmark, "Boundary conditions effects on non-reacting and reacting flows in a multiswirl combustor," *AIAA Journal*, vol. 44, no. 3, pp. 444–456, 2006.

[5] F. Vashahi, S. Lee, and J. Lee, "Experimental analysis of the swirling flow in a model rectangular gas turbine combustor," *Experimental Thermal and Fluid Science*, vol. 76, pp. 287–295, 2016.

[6] K. S. Reddy, D. N. Reddy, and C. M. Varaprasad, "Experimental and numerical investigations of swirling flows in a reverse flow gas turbine combustor," in *37th AIAA Fluid Dynamics Conference and Exhibit*, Miami, Florida, 2007.

[7] K. S. Reddy and D. N. Reddy, "Combustion studies in swirling flows in a reverse flow gas turbine combustor using CFD," in *38th Fluid Dynamics Conference and Exhibit*, Seattle, Washington, 2008.

[8] K. S. Reddy, D. N. Reddy, and C. M. Vara Prasad, "CFD analysis of fuel distribution in concentric swirling flows in a reverse flow gas turbine combustor," *ASME Turbo Expo 2006: Power for land, Sea, and Air*, 2006.

[9] S. Bharani, S. N. Singh, and D. P. Agrawal, "Effect of swirl on the flow characteristics in the outer annulus of a prototype reverse-flow gas turbine combustor," *Experimental Thermal and Fluid Science*, vol. 25, no. 6, pp. 337–347, 2001.

[10] S. Bharani, S. N. Singh, and D. P. Agrawal, "Effect of dump gap on velocity distribution and flow split in a prototype reverse-flow gas turbine combustor," *International Journal of Turbo & Jet Engines*, vol. 15, no. 2, 1998.

[11] S. K. Dhanuka, J. E. Temme, and J. Driscoll, "Unsteady aspects of lean premixed prevaporized gas turbine combustors: flame-flame interactions," *Journal of Propulsion and Power*, vol. 27, no. 3, pp. 631–641, 2011.

[12] G. J. Sturgess, J. Zelina, D. T. Shouse, and W. M. Roquemore, "Emissions reduction technologies for military gas turbine engines," *Journal of Propulsion and Power*, vol. 21, no. 2, pp. 193–217, 2005.

[13] H. C. Mongia, "N+3 and N+4 generation aeropropulsion engine combustors: part 6: operating conditions, target goals and lifted jets," in *49th AIAA/ASME/SAE/ASEE Joint Propulsion Conference*, San Jose, CA, 2013.

[14] C. Ruan, F. Chen, T. Yu, W. Cai, X. Li, and X. Lu, "Experimental study on flame/flow dynamics in a multi-nozzle gas turbine model combustor under thermo-acoustically unstable condition with different swirler configurations," *Aerospace Science and Technology*, vol. 98, article 105692, 2020.

[15] V. Burger, A. Yates, T. Mosbach, and B. Gunasekaran, "Fuel influence on targeted combustion properties part II: detailed results," *ASME turbo expo 2014: power for land, Sea and Air*, 2014.

[16] B. An, Z. Wang, and M. Sun, "Ignition dynamics and combustion mode transitions in a rocket-based combined cycle combustor operating in the ramjet/scramjet mode," *Aerospace Science and Technology*, vol. 118, article 106951, 2021.

[17] A. H. Lefebvre and J. H. Whitelaw, "Gas turbine combustion," *International Journal of Heat & Fluid Flow*, vol. 5, no. 4, pp. 228–228, 1984.

[18] J. F. Bourgouin, D. Durox, T. Schuller, J. Beaunier, and S. Candel, "Ignition dynamics of an annular combustor equipped with multiple swirling injectors," *Combustion & Flame*, vol. 160, no. 8, pp. 1398–1413, 2013.

[19] M. Philip, M. Boileau, R. Vicquelin et al., "Large Eddy Simulations of the ignition sequence of an annular multiple- injector combustor," *Proceedings of the Combustion Institute*, vol. 35, no. 3, pp. 3159–3166, 2015.

[20] K. Prieur, D. Durox, J. Beaunier, T. Schuller, and S. Candel, "Ignition dynamics in an annular combustor for liquid spray and premixed gaseous injection," *Proceedings of the Combustion Institute*, vol. 36, no. 3, pp. 3717–3724, 2017.

[21] W. Meier, X. R. Duan, and P. Weigand, "Investigations of swirl flames in a gas turbine model combustor: II. Turbulence–chemistry interactions," *Combustion & Flame*, vol. 144, no. 1, pp. 205–224, 2006.

[22] F. V. Tinaut, M. Reyes, B. Giménez, and J. V. Pastor, "Measurements of OH ∗ and CH ∗ Chemiluminescence in premixed flames in a constant volume combustion bomb under autoignition conditions," *Energy & Fuels*, vol. 25, no. 1, pp. 119–129, 2011.

[23] T. Yu, C. Ruan, F. Chen, Q. Wang, W. Cai, and X. Lu, "Measurement of the 3D Rayleigh index field _via_ time-resolved CH ∗ computed tomography," *Aerospace Science and Technology*, vol. 95, p. 105487, 2019.

[24] J. Miao, Y. Fan, T. Liu, and W. Wu, "Experimental and numerical study on thermodynamic characteristics in a Z-shaped evaporating pilot-flameholder," *Acta Astronautica*, vol. 162, no. C, pp. 56–65, 2019.

[25] K. Wang, F. Li, P. Zou, X. Lin, R. Mao, and X. Yu, "Effect of the fuel-air flow velocity on heat release rate of swirling non- premixed methane flames," *Aerospace Science and Technology*, vol. 95, p. 105465, 2019.

[26] B. Higgins, M. Q. Mcquay, and F. Lacas, "Systematic measurements of OH chemiluminescence for fuel-lean, high-pressure, premixed, laminar flames," *Fuel*, vol. 80, no. 1, pp. 67–74, 2001.

[27] Y. Hardalupas and M. Orain, "Local measurements of the time-dependent heat release rate and equivalence ratio using chemiluminescent emission from a flame," *Combustion & Flame*, vol. 139, no. 3, pp. 188–207, 2004.

[28] T. García-Armingol, Y. Hardalupas, A. M. K. P. Taylor, and J. Ballester, "Effect of local flame properties on chemiluminescence-based stoichiometry measurement," *Experimental Thermal and Fluid Science*, vol. 53, pp. 93–103, 2014.

[29] M. Orain and Y. Hardalupas, "Influence du combustible sur la mesure de richesse par chimiluminescence dans les flammes premelangees," *Comptes Rendus Mecanique*, vol. 338, no. 5, pp. 241–254, 2010.

[30] G. Hu, J. Li, W. Jin, J. Zhang, L. Yuan, and W. Zhai, "Experimental investigation on flow characteristics of a reverse-flow combustor," *International Journal of Aerospace Engineering*, vol. 2022, Article ID 4231002, 13 pages, 2022.

[31] J. Li, J. Chen, W. Jin, L. Yuan, and G. Hu, "The design and performance of a RP-3 fueled high temperature rise combustor based on RQL staged combustion," *Energy*, vol. 209, article 118480, 2020.

[32] A. Giannadakis, A. Naxakis, A. Romeos, K. Perrakis, and T. Panidis, "An experimental study on a coaxial flow with inner swirl: vortex evolution and flow field mixing attributes," *Aerospace Science and Technology*, vol. 94, p. 105373, 2019.

[33] G. Hu, J. Li, W. Jin, J. Z. Zhang, and L. Yuan, *Experimental Investigation of Flame Chemiluminescence and Flow Characteristics in a Reverse-Flow Combustor*, 2022.

[34] Y. Huang, X. He, H. Zhang, J. Wei, and D. W. M. Sng, "Spark ignition and stability limits of spray kerosene flames under subatmospheric pressure conditions," *Aerospace Science and Technology*, vol. 114, no. 32, article 106734, 2021.

[35] P. Jiang and X. He, "Performance of a novel mixed-flow trapped vortex combustor for turboshaft engine," *Aerospace Science and Technology*, vol. 105, article 106034, 2020.

[36] S. Yang, C. Zhang, Y. Lin, X. Xue, and X. Gan, "Experimental investigation of the ignition process in a separated dual-swirl spray flame," *Combustion and Flame*, vol. 219, pp. 161–177, 2020.